Catalysis Science & Technology

www.rsc.org/catalysis

Volume 3 | Number 12 | December 2013 | Pages 3073–3378

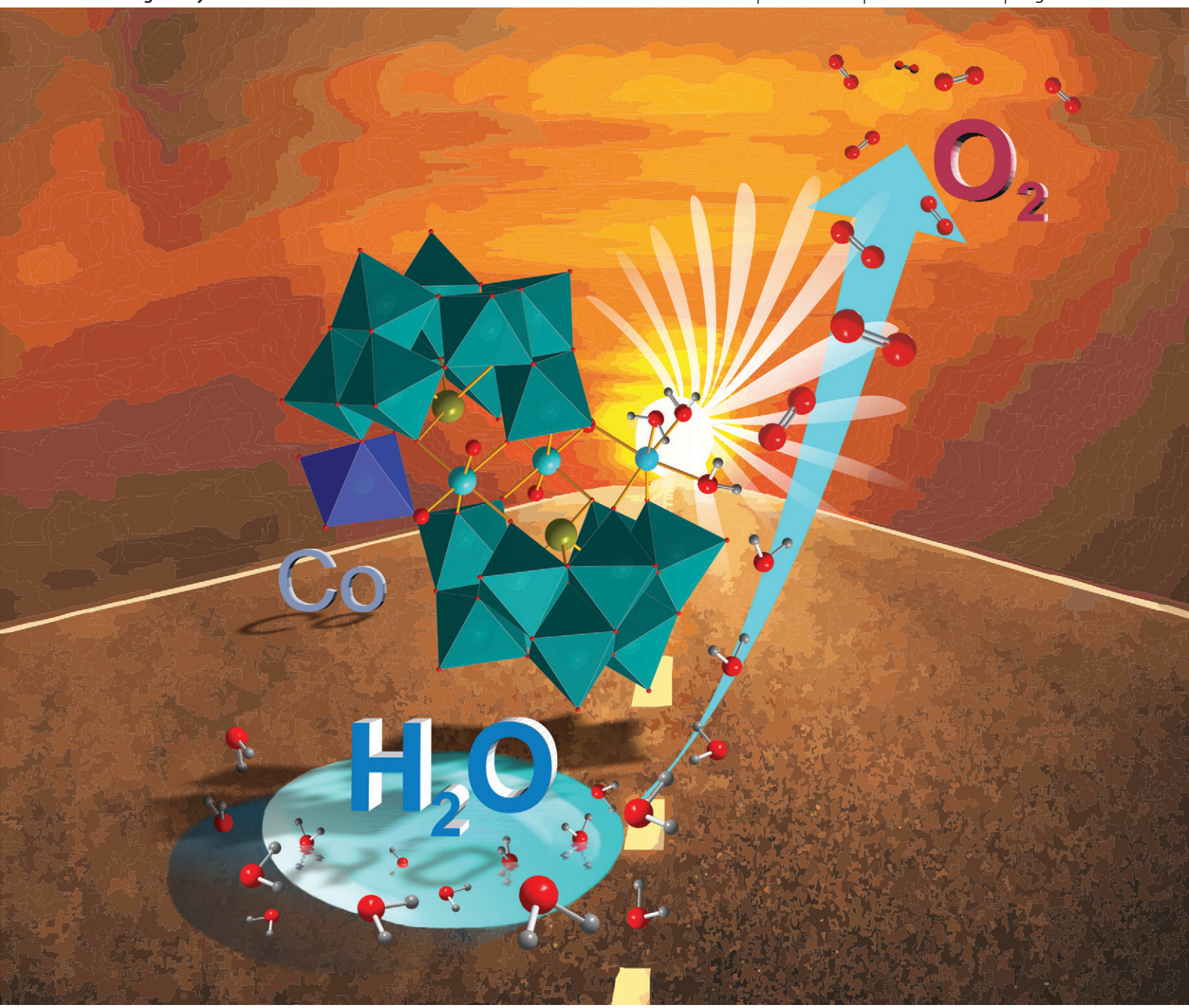

ISSN 2044-4753

RSC Publishing

COVER ARTICLE

Patzke *et al.*

Photocatalytic water oxidation with cobalt-containing tungstobismutates: tuning the metal core

2044-4753(2013)3:12;1-4

Catalysis
Science & Technology

RSC Publishing

PAPER

View Article Online
View Journal | View Issue

Cite this: *Catal. Sci. Technol.*, 2013, **3**, 3117

Photocatalytic water oxidation with cobalt-containing tungstobismutates: tuning the metal core†

Fabio Evangelisti, Pierre-Emmanuel Car, Olivier Blacque and Greta R. Patzke*

Received 5th July 2013,
Accepted 6th September 2013

DOI: 10.1039/c3cy00475a

www.rsc.org/catalysis

A new type of tungstobismutate water oxidation catalyst (WOC) with a disordered Co|W core, $[\{Co(H_2O)_3\}_2\{CoBi_2W_{19}O_{66}(OH)_4\}]^{10-}$ (**1**) was tested for visible-light-driven performance and compared to a series of isostructural Co- and Mn-containing polyoxometalates with variable transition metal contents, ($[Co_{2.5}(H_2O)_6\{Bi_2W_{19.5}O_{66}(OH)_4\}]^{8-}$ (**2**) and $[Mn_{1.5}(H_2O)_6\{Bi_2W_{20.5}O_{68}(OH)_2\}]^{6-}$ (**3**)). All compounds were structurally characterized, and no indications for significant decomposition under catalytic conditions for visible-light-driven water oxidation ($[Ru(bpy)_3]^{2+}$ as photosensitizer (PS) and $S_2O_8^{2-}$ as electron acceptor in different buffer systems) were found. For the first time, subtle differences in the core disorder patterns of isostructural POM-WOCs were revealed to be decisive for the catalytic activity of (**1**) (maximum TON of 21 with 97% oxygen yield for 115 μM (**1**)). Performance comparison of the POM series sheds new light on the structure–activity relationships for targeted POM-WOC construction. Indeed, the Co disorder differences between (**1**) and (**2**) exclusively affect the sterically more accessible external site of the two crystallographically independent Co core positions which has a 25% higher Co occupancy in (**1**). This points to a stereoselective reaction pattern for the tetranuclear POM core of WOC (**1**) which might open up novel construction strategies for the economic redesign of sandwich-type POM-WOCs. In parallel, we demonstrate for the POM series (**1**)–(**3**) that electrochemical measurements under catalytic conditions are a promising and convenient pre-screening strategy for WOC activity. Furthermore, POM/PS complex formation of (**1**) with $[Ru(bpy)_3]^{2+}$ is investigated in detail, and the different roles of Mn- and Co-centers in POM-WOC synthesis are compared.

Introduction

Artificial photosynthesis is a promising strategy to solve our worldwide energy and climate problems in a sustainable manner.[1] Water oxidation is the most challenging step in the process, and nature's cubane-related $\{Mn_3CaO_4\}$ core of Photosystem II (PS II) is by far the most inspirational motif for the design of water oxidation catalysts (WOCs).[2] This places polyoxometalate (POM) clusters, which are preferably formed by W, Mo and V in their highest oxidation states,[3] as structurally versatile hosts for a wide variety of tailored metal–oxo cores in the focus of current WOC research.[4] POM-WOC design is a complex multi-parameter task with structure–activity relationships (SAR) and catalyst stability as representative crucial issues.[5] We introduce a new efficient Co/Bi–POM-WOC, $[\{Co(H_2O)_3\}_2\{CoBi_2W_{19}O_{66}(OH)_4\}]^{10-}$, emerging from an isostructural series of sandwich-type Co- and Mn-POMs. Comparison of their WOC performance demonstrates that subtle variations of the metal-oxo core exert a tremendous influence on the observed catalytic activity. Special emphasis was placed on three essential criteria for efficient POM-WOC design: (1) SAR for POM core/shell construction, (2) POM/photosensitizer interactions and (3) WOC stability, *i.e.* drawing the line between homogeneous or heterogeneous catalysis.[6]

(1) First, the crucial importance of SAR for POM catalyst construction is evident from the wide variety of mainly empirically discovered Co-, Ni-,[7] and Ru-containing POM-WOCs with $[Co_4(H_2O)_2(PW_9O_{34})_2]^{10-}$ and $[\{Ru_4O_4(OH)_2(H_2O)_4\}(\gamma\text{-}SiW_{10}O_{36})_2]^{10-}$ among the most prominent examples.[8] The growing class of Co-POMs illustrates the present challenges particularly well. Although manifold new members of this POM family are being discovered,[9] only a small fraction of them are visible-light-driven WOCs with a preference for sandwich-type Co-POMs.[4h,10–13] Recently, however, a new Keggin-type $K_7[Co^{III}Co^{II}(H_2O)W_{11}O_{39}]$ WOC was reported, which amplified the family of POM-WOCs towards smaller mixed-valent clusters.[11] Comparison of this novel POM-WOC with Keggin-type analogues points to an essential interplay of the central $\{Co^{III}O_4\}$ unit with the catalytically active peripheral $\{Co^{II}O_6\}$

Institute of Inorganic Chemistry, University of Zurich, Winterthurerstrasse 190, CH-8057 Zurich, Switzerland. E-mail: greta.patzke@aci.uzh.ch; Fax: +41 44 635 6802; Tel: +41 44 635 4691

† Electronic supplementary information (ESI) available: Crystallographic data (ICSD 426302, 426303 and 426304) and BVS calculations for all compounds, powder X-ray diffraction patterns, FT-IR and UV/Vis spectra, TG measurements and cyclic voltammograms, experimental details for catalytic water oxidation, FT-IR and TG data for POM/PS complexes. See DOI: 10.1039/c3cy00475a

octahedron which is orientationally disordered.[11] Small molybdate clusters, such as $[CoMo_6O_{24}H_6]^{3-}$ and $[Co_2Mo_{10}O_{38}H_4]^{6-}$, have also been identified as promising WOCs, thus demonstrating that neither a critical POM size nor multi-site metal cores are mandatory for catalytic activity.[4k,12] Not only the key requirements for POM-WOC shell construction still remain unclear to a large extent, but the type and oxidation state of the POM belt atoms require further systematic SAR explorations as well. Ni-POMs serve as an example: whereas the $[Ni_5(OH)_6(OH_2)_3(Si_2W_{18}O_{66})]^{12-}$ polyanion with a clamshell-shaped geometry exhibits WOC activity,[7] the Ni-analogue of the catalytically active sandwich-type $[Co_4(H_2O)_2(SiW_9O_{34})_2]^{12-}$ does not show any WOC properties under analogous test conditions.[13] Mn-POMs are even more elusive targets for WOC construction: although PSII-inspired molecular Mn-WOCs attract a lot of attention, no efficient Mn-POM-WOCs have been reported so far to the best of our knowledge.[5b] This renders POM-WOC discovery a multi-parameter problem which has mostly been solved with empirical approaches to date.

(2) Next, the high negative charge of POMs poses another challenge for their combination with often positively charged photosensitizer (PS) molecules in homogeneous water oxidation systems. Crystalline POM hybrids of $[PW_{11}O_{39}]^{7-}$ and $[PW_{12}O_{40}]^{3-}$ with tris(bipyridine)ruthenium(III), $[Ru(bpy)_3]^{2+}$, one of the most widely used PS types, were first obtained through slow diffusion techniques.[14] Soon after, the model system $[\beta\text{-}Mo_8O_{26}]^{4-}/[Ru(tbbpy)(biH_2)]^{2+}$ confirmed the presence of supramolecular aggregates in solution.[15] Next, our studies into the $[Co_4(H_2O)_2(SiW_9O_{34})_2]^{12-}$ and $[\{Ru_3O_3(H_2O)Cl_2\}(SiW_9O_{34})]^{7-}$ POM-WOCs under catalytic conditions provided clear spectroscopic evidence for their formation of POM-PS complexes which could be recycled several times for new WOC runs.[13] Detailed flash photolysis investigations of primary interactions of $[\{Ru_4O_4(OH)_2(H_2O)_4\}(\gamma\text{-}SiW_{10}O_{36})_2]^{10-}$ with $[Ru(bpy)_3]^{2+/3+}$ pointed to static quenching in POM/PS ion paired species (ratios *ca.* 1/4) as an adverse process in the photocatalytic cycle.[16] In contrast, POM/PS hybrid complex formation with $[Ru(bpy)_3]^{2+}$ has recently been applied as a synthetic concept to construct new WOCs from the polyoxomolybdates $[Mo_6O_{19}]^{2-}$, $[Mo_5S_2O_{23}]^{4-}$ and $\alpha\text{-}[Mo_8O_{26}]^{4-}$.[17] The complexity of these observations demonstrates that POM/PS interactions require detailed studies for each newly found POM-WOC.

(3) Finally, the high structural flexibility of POMs often comes at the expense of their stability. Possible metal leaching from the core region might give rise to subsequent formation of an active nanoparticular catalyst, as recently postulated for the formation of CoO_x nanocatalysts from $[Co_4(H_2O)_2(PW_9O_{34})_2]^{10-}$ as a precatalyst under electrochemical conditions.[18] In parallel, laser flash photolysis studies on $[Co_4(H_2O)_2(PW_9O_{34})_2]^{10-}$ under visible-light-driven water oxidation conditions indicated that the Co-POM serves as a precatalyst for an active molecular species.[19] Most recent electrochemical studies on this model Co-POM-WOC finally revealed that subtle variations of the reaction conditions for micro- and nanomolar amounts of catalyst species render the true WOC extremely difficult to assign, *i.e.* the distinction between homo- and heterogeneous catalysis reaches the limits of standard analytical methods.[20] Targeted applications of POMs as heterogeneous electrocatalysts, such as $[Co_9(H_2O)_6(OH)_3(HPO_4)_2(PW_9O_{34})_3]^{16-}$ on carbon paste electrodes, are an elegant alternative.[21] However, the search for genuinely homogeneous POM-WOCs and related molecular catalysts remains essential for understanding their reaction pathways through *in situ* spectroscopy[22] and theoretical calculations[23] on the way to clear-cut SAR for informed design.

In the following, we introduce $[\{Co(H_2O)_3\}_2\{CoBi_2W_{19}O_{66}(OH)_4\}]^{10-}$ (Co/Bi-POM (**1**)) as a POM-WOC with high stability under visible-light-driven water oxidation conditions. Unexpectedly, systematic comparison of Co/Bi-POM (**1**) with isostructural POMs showed that neither the closely related Co-POM $[Co_{2.5}(H_2O)_6\{Bi_2W_{19.5}O_{66}(OH)_4\}]^{8-}$ nor its Mn-POM analogue, $[Mn_{1.5}(H_2O)_6\{Bi_2W_{20.5}O_{68}(OH)_2\}]^{6-}$, are active WOCs. The outstanding catalytic properties of Co/Bi-POM (**1**) among the series were investigated with a variety of analytical methods and reference experiments in search of the active catalytic species. The results shed new light on guidelines for systematic POM-WOC construction.

Results and discussion

Synthetic parameters

Three isostructural sandwich POMs with disordered $M^{2+}|W$ cores were obtained from solution methods through systematic variations of literature protocols in order to compare the influence of cores with different $Co^{2+}|W$ ratios to $Mn^{2+}|W$ cores on the catalytic activity.[24,25] Replacement of pure aqueous media by acetate solutions (pH 4.5, 40 mM) was applied to access two isostructural sandwich-type Co-POMs, namely $Na_{10}[\{Co(H_2O)_3\}_2\{CoBi_2W_{19}O_{66}(OH)_4\}]\cdot 37H_2O$ (Co/Bi-POM (**1**)) and $Na_8[Co_{2.5}(H_2O)_6\{Bi_2W_{19.5}O_{66}(OH)_4\}]\cdot 32H_2O$ (Co/Bi-POM (**2**)). Their isostructural Mn-analogue $Na_6[Mn_{1.5}(H_2O)_6\{Bi_2W_{20.5}O_{68}(OH)_2\}]\cdot 36H_2O$ (Mn/Bi-POM (**3**)) was obtained from the same protocol[24] by replacing the Co-based precursor with $MnSO_4\cdot 2H_2O$. In the following, crystal structures of compounds (**1**)–(**3**) are discussed in detail and compared to the present state of investigations on this POM type.

Structure of $Na_{10}[\{Co(H_2O)_3\}_2\{CoBi_2W_{19}O_{66}(OH)_4\}]\cdot 37H_2O$ (Co/Bi-POM (1))

The sandwich-type Co/Bi-POM (**1**) crystallizes in the triclinic space group $P\bar{1}$ (Table S1†). The two identical lacunary $\beta\text{-}\{BiW_9O_{33}\}$ units of the $[\{Co(H_2O)_3\}_2\{CoBi_2W_{19}O_{66}(OH)_4\}]^{10-}$ polyanion are connected *via* two disordered $\{WO_2|CoO_2\}$ groups W(10)|Co(2) and two $\{Co(H_2O)_3\}$ (Co(1)) moieties which form the tetranuclear metal core. The two crystallographically equivalent internal atoms of the core display disorder which was refined with a model based on site occupancies of 50% W(10) and 50% Co(2) which are in agreement with elemental analysis and overall charge balance.

The central Bi atoms of Co/Bi-POM (**1**) exhibit pyramidal environments consisting of a basal plane with three Bi–O

bonds (2.130(6) to 2.154(6) Å) and a lone pair at the top of the pyramid. All of the non-disordered tungsten atoms are octahedrally coordinated with W–O bond distance ranges of 1.766(7)–2.083(7) Å for equatorial W···O bonds. The longer internal W···O bond distances range from 2.209(7) to 2.320(7) Å, whereas the external W···O bonds are characteristically short (1.726(8) and 1.771(7) Å). Intermetallic W···W distances range from 3.2848(6) to 3.3880(6) Å for the edge-sharing WO_6 octahedra and from 3.6708(7) to 3.7097(9) Å for the corner-sharing WO_6 polyhedra, respectively.

The disordered W(10)|Co(2) sites are octahedrally coordinated by six oxygen atoms with metal-oxygen distances in the 1.893(9)–2.112(8) Å range and intermetallic distances between 3.5461(8) and 3.8728(10) Å for corner-sharing W|Co···W octahedra. The remaining two terminal $\{Co(H_2O)_3\}$ (Co(1)) units of the tetranuclear core show longer Co···OH_2 bonds (2.088(8)–2.211(7) Å) than Co···O bonds (2.030(7)–2.070(7) Å). Interatomic distances between corner-sharing Co···W octahedra are in the expected range (3.5435(18) to 3.7862(15) Å).

Five crystallographically independent and fully occupied Na positions were located in the course of the refinement (Na(1), Na(2), Na(3), Na(4), Na(5)). They are coordinated by oxygen atoms of the polyoxoanion or by crystal water molecules. Their coordination numbers increase from 3 (Na(5)) over 6 (Na(1), Na(2), Na(3)) to 7 (Na(4)) with Na···O bond lengths ranging from 2.18(2) to 2.88(1) Å. Several aqualigands complete the environment of Co/Bi-POM (**1**).

Bond valence sum (BVS) values[26] for all tungsten atoms (5.8–6.1) agree well with the common W oxidation state of +6 in POMs. Bi is present in the +3 oxidation state according to its BVS of 3.05. The BVS value of 1.7 for Co(1) indicates the presence of Co^{2+}. Most oxygen atoms of Co/Bi-POM (**1**) have BVS values corresponding to an oxidation state of −2 (between 1.4 and 2.1), except for O(33), O(34), O(35), O(36) and O(37). BVS values of 0.28, 0.32 and 0.34 for O(33), O(34) and O(35), respectively, identify them as terminal H_2O molecules. According to their medium BVS values (0.8 and 0.7), O(36) and O(37) are bridging hydroxo groups.

Structure of $Na_8[Co_{2.5}(H_2O)_6\{Bi_2W_{19.5}O_{66}(OH)_4\}]\cdot 32H_2O$ (Co/Bi-POM (**2**))

Co/Bi-POMs (**1**) and (**2**) have the same POM architecture in common, *i.e.* they both consist of two identical lacunary β-$\{BiW_9O_{33}\}$ shells which are connected through a Co|W tetranuclear metal core. Co/Bi-POM (**2**), however, crystallizes in the monoclinic space group $P2_1/n$ (Table S1†). Analogous to Co/Bi-POM (**1**), the tetranuclear metal core of (**2**) displays disorder as well. Other than in (**1**), both crystallographically independent core metal positions of Co/Bi-POM (**2**) are disordered. Refinement of this disordered model resulted in occupancies of 50% W(10)|Co(1) and 75/25% Co(2)|W(11), respectively. Bismuth displays the same pyramidal oxygen coordination environment with related bond distances (2.122(8), 2.135(8) and 2.148(8) Å) as described for (**1**) above. Likewise, all tungsten centers of (**2**) are octahedrally coordinated with medium bond lengths (1.780(9)–2.068(8) Å) for the equatorial W···O bonds, long internal W···O bonds (2.198(7)–2.301(8) Å) and short external W···O distances (1.714(8)–1.756(8) Å). W···W contacts range from 3.2770(9) to 3.3561(11) Å for edge-sharing WO_6 moieties and from 3.6610(10) to 3.7095(10) Å for the corner-sharing WO_6 octahedra.

The disordered core metal sites W(10)|Co(1) and Co(2)|W(11) are both octahedrally coordinated with oxygen atoms which exhibit bond distance ranges of 1.863(1)–2.113(9) Å and 1.967(1)–2.108(8) Å, respectively. All intermetallic distances (W(10)|Co(1), Co(2)|W(11) and fully occupied tungsten atoms) cover a range from 3.498(19) to 3.913(8) Å.

The surroundings of Co/Bi-POM (**2**) are constituted by crystal water molecules, three fully occupied Na positions and two 50% occupied Na positions. Refinements revealed an increase of Na coordination numbers from 3 (Na(5)) over 4 (Na(4)) to 6 (Na(1), Na(2), Na(3)) with Na···O bond distances between 2.310(19) and 2.825(16) Å.

BVS values between 5.83 and 6.09 for all tungsten atoms clearly point to an oxidation state of +6 throughout, and the BVS value of 3.05 for Bi corresponds well with the expected oxidation state of +3. All oxygen atoms exhibit BVS values between 1.4 and 2.1 suggesting an oxidation state of −2, except for lower values for O(30), O(33), O(35), O(36) and O(37) (0.9, 0.9, 0.7, 0.5 and 0.6, respectively). The two values of 0.9 for O(30) and O(33) indicate the presence of hydroxo groups, while the values of 0.5, 0.6 and 0.7 for O(36), O(37) and O(35) are characteristic for water molecules.

Structure of $Na_6[Mn_{1.5}(H_2O)_6\{Bi_2W_{20.5}O_{68}(OH)_2\}]\cdot 36H_2O$ (Mn/Bi-POM (**3**))

Mn/Bi-POM (**3**) is isostructural with the Co/Bi-POMs (**1**) and (**2**), and it crystallizes in the monoclinic space group $P2_1/n$ (Table S1†). The β-$\{BiW_9O_{33}\}$ building blocks sandwich a tetranuclear Mn|W core, and both of its crystallographically independent positions are disordered. Other than in compounds (**1**) and (**2**), the terminal metal position displays more pronounced disorder than the internal sites: occupancies were refined to 90|10% for W(10)|Mn(1) and to 35|65% for W(11)|Mn(2) (Fig. 1). Nine different oxygen atoms of (**3**) form terminal W···O bonds of the octahedral $\{WO_6\}$ building blocks (distances between 1.704(16) and 1.740(13) Å), and three oxygen positions form connecting internal bonds with notably longer distances (2.214(12) to 2.299(13) Å). The octahedral coordination of the nine fully occupied tungsten positions is completed by oxygen atoms in equatorial positions with bond lengths ranging from 1.784(15) to 2.056(16) Å. The W···W distances within the lacunary β-$\{BiW_9O_{33}\}$ units range from 3.6654(11) to 3.6998(11) Å for corner-sharing and from 3.2712(11) to 3.3514(11) Å for edge-sharing $\{WO_6\}$ octahedra, respectively.

The tungsten centers of the disordered W(10)|Mn(1) and W(11)|Mn(2) sites are octahedrally coordinated with W···O bond lengths ranging between 1.76(2) to 2.186(13) Å, associated to interatomic metal cation distances between 3.5518(13)

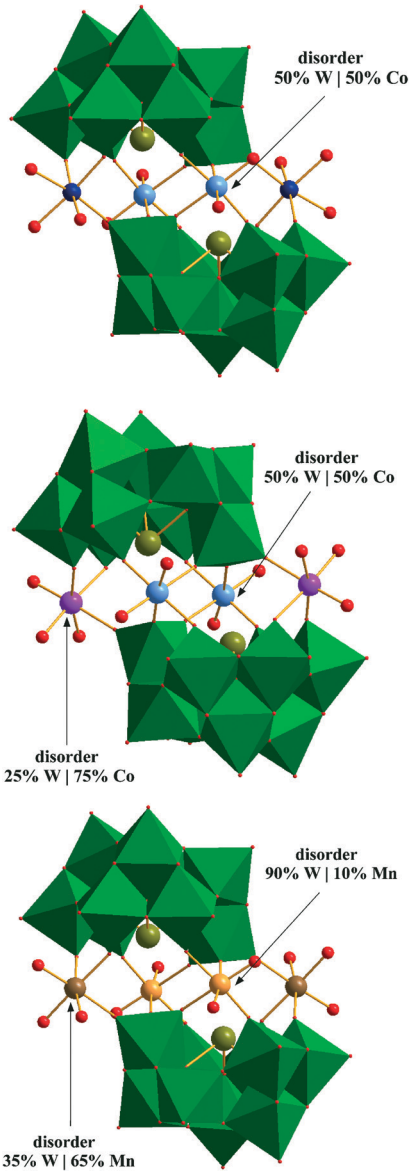

Fig. 1 Polyhedra and ball-and-stick representations (WO_6 = green, O = red) of Co/Bi-POM (**1**) (top; Co = dark blue, W|Co = light blue), Co/Bi-POM (**2**) (middle; 50W|50Co = light blue, 25W|75Co = pink) and Mn/Bi-POM (**3**) (bottom; 90W|10Mn = orange, 35W|65Mn = brown).

and 3.9239(13) Å for corner-sharing $WO_6|MnO_6\cdots WO_6$ octahedra.

As observed for the Co/Bi-POMs (**1**) and (**2**), the pyramidal coordination of the Bi heteroatoms is constituted by a lone electron pair oriented towards the tetranuclear metal core and three oxygen atoms with Bi···O distances of 2.131(13), 2.142(13) and 2.147(12) Å.

Mn/Bi-POM (**3**) is surrounded by three Na positions which are all fully occupied and octahedrally coordinated with Na···O bond lengths ranging between 2.32(3) and 2.64(5) Å. Crystal water molecules complete the surroundings of the $[Mn_{1.5}(H_2O)_6\{Bi_2W_{20.5}O_{68}(OH)_2\}]^{6-}$ polyanion. All tungsten BVS values (5.88 to 6.15) clearly indicate an oxidation state of +6, and the BVS value of 3.16 for Bi is in line with Bi^{3+}.

Oxygen BVS values of (**3**) are in the range for −2 oxidation states (between 1.5 and 2.1), except for O(34), O(35), O(36), O(37) and O(38). Lower BVS values (0.61, 0.45 and 0.49) identify O(36), O(37) and O(38) as terminal water molecules, whereas medium BVS values of 1.4 and 1.3 for O(34) and O(35), respectively, suggest the presence of hydroxo groups.

Phase purity of representative Co/Bi-POM (**1**), Co/Bi-POM (**2**) and Mn/Bi-POM (**3**) samples was investigated with PXRD measurements (Fig. S1–S3†). The related PXRD patterns are in line with the isostructural POM series, and the experimental data agree with the calculated theoretical patterns.

Our results on Co/Bi-POMs (**1**) and (**2**) confirm the strong tendency towards Co|W core disorder which has previously been observed for the isostructural POM $Na_{(10-4x)}[Bi_2W_{(20+x)}Co_{(2-x)}O_{70}(H_2O)_6]\cdot 41H_2O$ (x = 0.28) with intermediate cobalt content compared to (**1**) and (**2**).[25] This may indicate a certain phase width for Co|W cores with variable compositions, and further studies into the synthetic parameters are under way. Furthermore, high quality single crystal growth of $Na_{10}[Bi_2W_{20}Co_2O_{70}(H_2O)_6]\cdot 30H_2O$ and $Na_{10}[Bi_2W_{20}Mn_2O_{70}(H_2O)_6]\cdot 26H_2O$, respectively, was not possible *via* a related protocol, so that no detailed crystallographic data were reported for these compounds.[24] Furthermore, ICSD data for the Na/K-containing analogue of Mn/Bi-POM (**3**) with 68% Mn on the terminal sites (100% W on the internal sites) are related to the above mentioned disorder pattern of the Mn sites.[27] Nevertheless, crystallographic evidence for $[Bi_2W_{20}M_2O_{70}(H_2O)_6]^{10-}$ (M = Mn, Co) with fully occupied M sites is missing to date, and the present data clearly suggest that metal core disorder is a characteristic property of this sandwich-type tungstobismutate type.

Cyclic voltammetry of POMs (1)–(3)

Generally, electrochemical characterization of sandwich-type polyoxotungstates in aqueous solutions by cyclic voltammetry (CV) is strongly pH dependent. In the negative potential range, 2–4 processes involving tungsten centers can be observed which are particularly evident in acidic media (0.4 M NaOAc/HOAc buffer at pH 3, *cf.* Fig. S6†). All compounds were furthermore studied under catalytic conditions at pH 5.8 in silicate buffer (20 mM $Na_2SiF_6/NaHCO_3$) to enhance the otherwise weakly developed redox waves of Co^{II}. For stability tests of Co/Bi-POM (**1**), combined CV and UV/Vis measurements were performed on aged solutions which were stored for 24 h under ambient conditions. No significant changes in cyclic voltammograms and UV/Vis spectra were observed after the ageing process.

Cyclic voltammograms of Co/Bi-POM (**1**) in 0.4 M H_2SO_4 (pH 3) (Fig. S6†) display defined oxidation peaks of the W^{6+}/W^{5+} couple at −0.060 V, −0.104 V and −0.240 V together with an associated but less defined reduction peak at −0.670 V. The Co^{2+}/Co^{3+} redox couple shows a quasi-reversible wave with an oxidation peak at +0.965 V and a rather undefined reduction peak. The observed peak broadening may point

to a sum of a pairs of bands which are undergoing a two electron oxidation process.

It is well known from literature that only monosubstituted POMs and $[Co_x^{II}W_{11-x}O_{40}]^{6-}$ display an electroactive Co center.[28] CV measurements in protic solvents may afford asymmetric electrochemical patterns with much larger anodic than cathodic branches. These phenomena are often related to water oxidation processes occurring at the glassy carbon surface,[29] and they are reinforced at pH values of the supporting electrolyte which are close to catalytic conditions, thereby excluding reliable assignment of electrons to different redox waves of the metal centers.

The Co^{2+}/Co^{3+} redox couple of Co/Bi-POM (**1**) in catalytic buffer medium (20 mM $Na_2SiF_6/NaHCO_3$, pH 5.8, *cf.* Fig. 2) displays less defined oxidation peaks in the positive region at +0.623 V (I) and +0.934 V (II) together with associated reduction peaks at +0.743 V (II') and +0.607 V (I'). The redox processes can be assigned to the two different intermediates $2(Co^{II}{}_3)/2(Co^{II}{}_2Co^{III})$.[30] The negative domain (Fig. S7†) displays two characteristic wave pairs of the W^{6+} centers with different intensities at −0.135 V and −0.328 V for the oxidation process and at −0.160 V and −1.009 V for the reduction process, respectively. These intensity differences are due to the different numbers of involved electrons, *i.e.* 2 electrons for the −1.009 /−0.328 V couple and one electron for the −0.160/−0.135 V couple.[28a]

In comparison, Co/Bi-POM (**2**) shows less defined and convoluted W oxidation waves in the negative domain at −0.546 V, −0.361 V and −0.271 V which are accompanied by reduction waves located at −0.718 V and −0.595 V (Fig. S7†). The observed oxidation processes of Co^{II} are in line with literature:[31] a broadened and rather undefined oxidation wave at +0.852 V (III) corresponds to the respective reduction at +0.648 V (III') (Fig. S7†). We would like to point out that Co centers in POMs are generally difficult to monitor with CV methods which renders their observed response in (**1**) and (**2**) under catalytic conditions truly significant and selective.[32]

Cyclic voltammograms of Mn/Bi-POM (**3**) (Fig. 3) showed a broad reduction wave of the tungsten centers in the negative

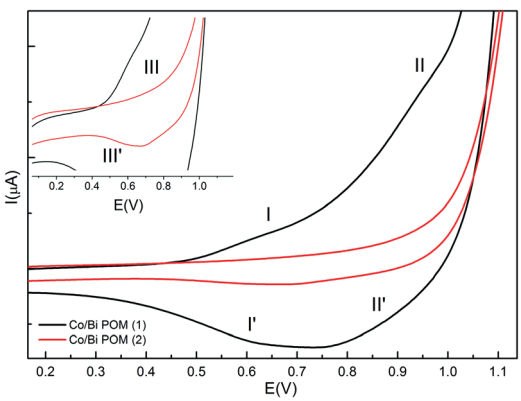

Fig. 2 Cyclic voltammograms of Co/Bi-POM (**1**) (15.8 mM – black line) and Co/Bi-POM (**2**) (15.8 mM – red line) in $Na_2SiF_6/NaHCO_3$ buffer (20 mM) at pH 5.8; scan rate: 10 mV s^{-1}, (*vs.* Ag/AgCl). Insert: magnification of Co/Bi-POM (**2**).

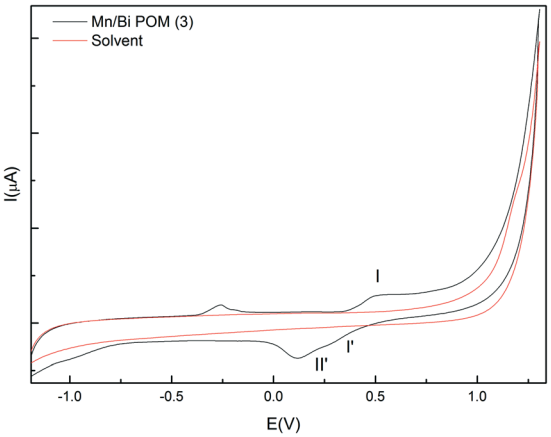

Fig. 3 Cyclic voltammograms of Mn/Bi-POM (**3**) (30 mM) in $Na_2SiF_6/NaHCO_3$ (20 mM) buffer at pH 5.8; scan rate: 10 mV s^{-1}, (*vs.* Ag/AgCl).

range at −0.962 V which can be interpreted as a convolution of two processes. One re-oxidation peak at −0.256 V is associated with the first reduction wave and the 70 mV peak potential difference corresponds to a reversible one electron redox transfer.[28a] However, the re-oxidation wave corresponding to the second reduction process displays a more complex splitting pattern with another wave located at −0.186 V. The Mn^{2+}/Mn^{3+} couple in the positive scan range displays a potential difference of +0.409 V (oxidation: +0.536 V, reduction: +0.127 V). There is also indication of a second Mn^{2+}/Mn^{3+} redox couple with weak peaks appearing at +0.427 V and at +0.295 V with a more defined shoulder (I–I',II'), respectively. In line with literature data for Mn-POMs, these redox couples are related to one-electron Mn^{2+}/Mn^{3+} transfer processes between different Mn sites of the POM moiety.[33] Computational studies and more detailed electrochemical investigations (controlled-potential electrolysis and coulometry) are currently in progress.

Spectroscopic and stability investigations

Stability tests of POMs (**1**)–(**3**) in catalytic media (Na_2SiF_6 buffer at pH 5.8 and NaPi buffer at pH 8) were conducted with UV/Vis spectroscopy. Co/Bi-POM (**1**) shows two characteristic bands in $NaSiF_6$ media assigned to O_d–W charge transfer (< 450 nm) and to the $^4T_{1g}(P) \rightarrow {}^4T_{1g}(F)$ transition of octahedral Co^{2+} at 543 nm, respectively.[32b,34] Most importantly, spectra of (**1**) recorded after 3 h of ageing in catalytic media did not show significant intensity decreases of the above Co absorption bands and a slight intensity loss (<5%) was only observed after 12 h (Fig. 4). Based on this evidence, we conclude that POM-WOC (**1**) enters the photocatalytic cycle as a structurally intact active species with no substantial decomposition or side product formation processes involved.[32b] Similar to (**1**), UV/Vis spectra of Co/Bi-POM (**2**) display a O–W charge transfer band in the higher energy region (above 370 nm) as well as the Co^{2+} related $^4T_{1g}(P) \rightarrow {}^4T_{1g}(F)$ transition at 543 nm. A third absorption band around 490 nm might indicate Jahn–Teller distortion of the

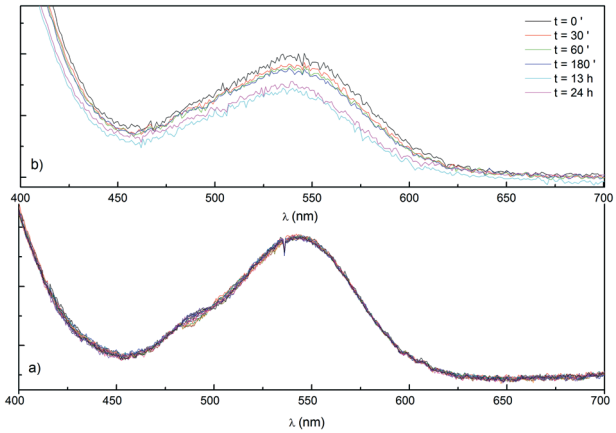

Fig. 4 Time-dependent UV/Vis absorption spectra of (a) Co/Bi-POM (**2**) (70 μM) and (b) Co/Bi-POM (**1**) (50 μM) (final recording after 24 h) in Na_2SiF_6/$NaHCO_3$ buffer (30 mM, pH 5.8).

octahedrally coordinated Co centers.[46a] Likewise, Co/Bi-POM (**2**) remained stable after 2 h of exposure to catalytic conditions with Na_2SiF_6 buffer.

Concerning stability tests in NaPi media, Co/Bi-POM (**1**) did not show any intense absorption bands, whereas spectra of (**2**) are virtually identical to those recorded in Na_2SiF_6 buffer (Fig. S8†).

UV/Vis spectra of Mn/Bi-POM (**3**) in catalytic buffer media exhibit an intense O–W charge transfer peak below 293 nm. Another broad band around 390–400 nm indicates the presence of Mn^{2+},[47] whereas the typical bands of Mn^{3+} and Mn^{4+} in the 450–500 nm range were absent.[35] Given that no significant intensity loss after 24 h of ageing was observed, the Mn-containing sandwich type POM (**3**) is assumed to be stable under catalytic test conditions.

Visible light-driven water oxidation

Visible-light-driven water oxidation activity of POMs (**1**)–(**3**) was investigated according to standard literature protocols[13,36] (for details *cf.* Experimental) with $[Ru(bpy)_3]^{2+}$ as photosensitizer (PS) and $S_2O_8^{2-}$ as a sacrificial electron acceptor in different buffer media: NaOAc/HOAc (40 mM, pH 4.7), NaPi (40 mM, pH 7 and 8), and Na_2SiF_6/$NaHCO_3$ buffer (20 mM, pH 5.8). Na_2SiF_6 buffer offers the advantage of reducing the radical decomposition of the Ru-PS.[37]

Catalytic performance was evaluated with special emphasis on (a) turnover number (TON) expressing the ratio between total molar amount of O_2 produced and number of Co centers involved in the catalytic cycle, and (b) yield (per $S_2O_8^{2-}$), based on a maximum oxygen yield corresponding to half of the initial molar $S_2O_8^{2-}$ concentration. A precise description of the applied calibration and Clark electrode techniques can be found in the ESI† (*cf.* also Fig. S10–11).

Interestingly, only Co/Bi-POM (**1**) exhibited catalytic water oxidation activity in Na_2SiF_6 media, whereas compounds (**2**) and (**3**) remained inactive under the applied test conditions. The catalytic performance parameters of (**1**) were investigated in detail.

Co/Bi-POM (**1**) exhibits water oxidation activity in the concentration range from 62 μM to 400 μM, and maximum TON (21) with 97% oxygen yield were observed for 115 μM. This oxygen yield is rather high in comparison with comparable Co-POM WOCs under related catalytic conditions.[38] At 166 μM, POM-WOC (**1**) afforded the highest molar O_2 production (28.7 μmol, 97% yield; *cf.* Fig. 5). This is in stark contrast to the observed catalytic inactivity of (**2**) over the same concentration range (62 μM–400 μM, *cf.* Fig. S11 and S14†), because both compounds differ only with respect to the disorder on the W|Co sites (Fig. 1). For the optimal concentration (166 μM) of the active POM-WOC (**1**), the initial turnover frequency (TOF) was determined as 0.9 min^{-1}.

Concentration screening of Co/Bi-POM WOC (**1**) is in line with previously reported trends.[11,36] Gradual increase of the POM concentration leads to maximum POM-WOC efficiency at 166 μM for Co/Bi-POM WOC (**1**). However, higher POM concentrations above this optimal working point induce a significant decline in catalytic activity (Fig. 5, Table 1), *e.g.* O_2 yields decrease from 76% (16 μmol) for 255 μM of (**1**) to 26% (5.6 μmol for 400 μM (**1**)), respectively. This trends clearly shows that POM-WOC concentration is a key optimization parameter.

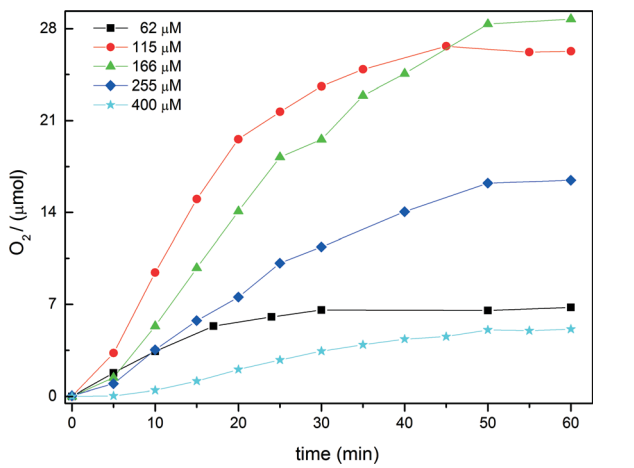

Fig. 5 Kinetic monitoring (GC) of O_2 formation from photocatalytic water oxidation with Co/Bi-POM (**1**). Conditions: LED lamp, 470 nm; 1 mM $[Ru(bpy)_3]Cl_2$, 5 mM $Na_2S_2O_8$, Na_2SiF_6 buffer pH 5.8 (20 mM) [cyan star: 400 μM, black square: 62 μM, blue prism: 255 μM, green triangle: 166 μM, red circle: 115 μM].

Table 1 WOC efficiency of Co/Bi-POM (**1**) under different catalytic conditions (1 mM $[Ru(bpy)_3]Cl_2$, 5 mM $Na_2S_2O_8$ and different amounts of (**1**) in 20 mM Na_2SiF_6 at pH 5.8)

(**1**) (μM)	O_2 (μmol)	Yield (%)	TON
62	6.8	36	10
115	26.3	97	21
166	28.7	97	16
255	16.5	77	6
400	5.7	26	2

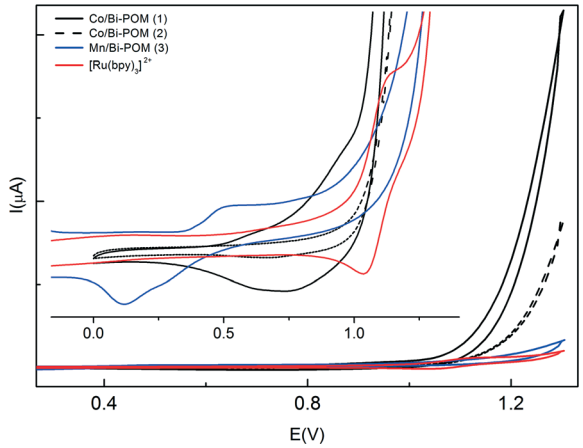

Fig. 6 Cyclic voltammograms of Co/Bi-POMs (**1**) (black) and (**2**) (dashed black), and of Mn/Bi-POM (**3**) (blue); conditions: 1 mM $[Ru(bpy)_3]Cl_2$ in $Na_2SiF_6/NaHCO_3$ (20 mM) buffer at pH 5.8; scan rate: 10 mV s^{-1} (*vs.* Ag/AgCl). Main picture: water oxidation current flow for Co/Bi-POM (**1**) (inset: magnification 0–1.2 V range).

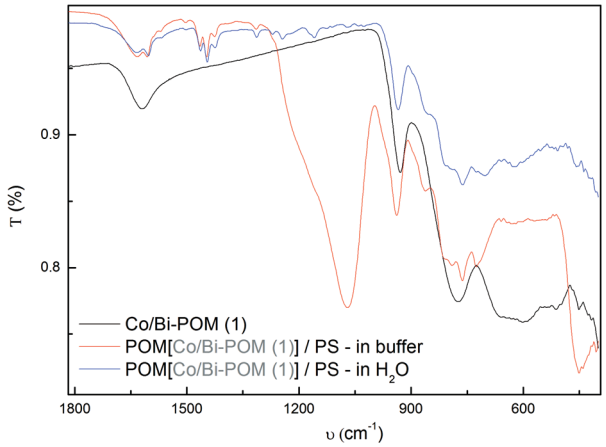

Fig. 8 FT-IR spectra of pristine (**1**) (black), POM-PS (**1**) complex synthesized from Na_2SiF_6 buffer medium (red) and POM-PS (**1**) complex obtained from H_2O (blue).

Ion pairing between the highly negatively charged Co/Bi-POM (**1**) and the positively charged $[Ru(bpy)_3]^{2+}$ PS is occurring over the entire POM concentration range from 62 μM onwards and can be observed as formation of a dark orange colloidal suspension of the POM-PS complex as reported in our previous work.[13] POM-PS complex formation becomes more evident for higher POM concentrations and seems to be an integral part of the catalytic process. However, the precise structure of these ion associates in solution remains to be further elucidated.

The POM-PS complex of (**1**) has been studied with various analytical techniques, including FT-IR (Fig. 7–8 and S15†) and TG (Fig. 9), as outlined in the next sections. Furthermore, the influence of different catalytic parameters on the WOC efficiency of (**1**) was investigated. First, the $S_2O_8^{2-}$ concentration was varied between 2.5 and 9 mM and all other parameters were kept constant. We observed that the standard 5 mM concentration for catalytic tests leads to maximum O_2 production rates. Higher and lower persulfate concentrations decrease the O_2 yields and no O_2 evolution was detected in the absence of $S_2O_8^{2-}$ (*cf.* also Table S8†).

Analogous tests were performed to investigate the influence of the $[Ru(bpy)_3]Cl_2$ concentration parameter in the range from 0 mM to 2 mM. Again, the standard 1 mM PS concentration applied for catalytic tests afforded maximum oxygen yield, and no O_2 evolution occurred in the absence of PS (Table S8†). POM-PS complex formation was observed over the entire PS concentration range, and the amounts formed were determined to be approx. the same for (**1**) and (**2**) after centrifugation and subsequent drying at room temperature under N_2 atmosphere. Obviously, stoichiometric complex formation is reached at 0.5 mM PS concentration, and further investigations are under way to determine if excess PS would accelerate WOC oxidation.

Detailed kinetic evaluations of Co/Bi-POM (**1**) are difficult, because the correlation between WOC concentration and O_2 evolution appears to be rather complex. Whereas oxygen formation reaches its maximum for medium POM-WOC concentrations (around 166 μM), the reaction rate apparently

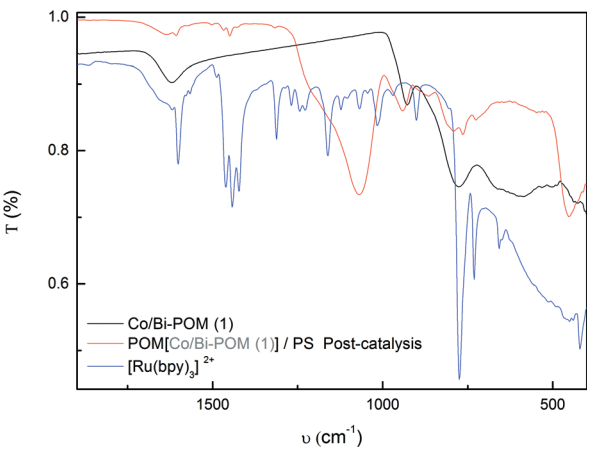

Fig. 7 FT-IR spectra of pristine (**1**) (black), POM-PS (**1**) complex recovered from Na_2SiF_6 buffer media after catalytic tests (red) and $[Ru(bpy)_3]Cl_2$ (blue).

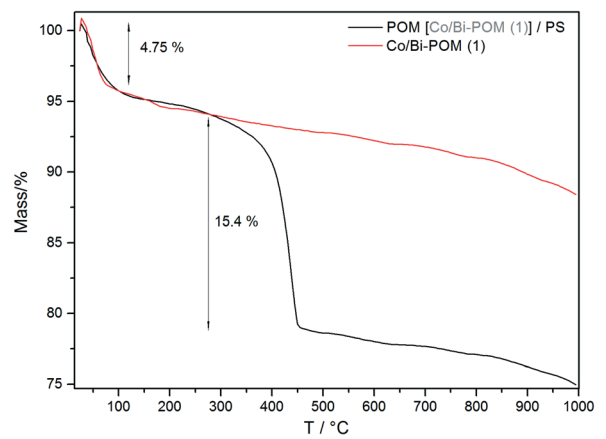

Fig. 9 TG curves of (**1**) (red) and POM-PS (**1**) complex recovered from Na_2SiF_6 media after catalytic tests (air, Al_2O_3 crucible, heating rate 10 K min^{-1}).

declines again for higher WOC concentrations (255 μM and 400 μM). A follow-up study is in progress to establish a coherent kinetic model correlating POM-PS complex formation with the concentration-dependent reaction rates.

Catalyst stability tests

Stability of POM-WOC catalysts against leaching of metal cations which might form secondary – and possibly heterogeneous – active species is a key design criterion for artificial photosynthesis processes.[18,39] UV/Vis experiments (*cf.* above) indicate stability of the Bi-POMs (**1**)–(**3**) under the applied catalytic conditions.

The formation of free Co^{2+} species was furthermore excluded on the basis of CV measurements of $Co(NO_3)_2$ solutions at different concentrations (5–20% of the above WOC concentrations, *i.e.* 15.8–50 mM under standard conditions with Na_2SiF_6 buffer). These reference solutions show Co redox waves at 0.652 V/0.464 V and 0.973 V/0.774 V (see Fig. S7†), *i.e.* they display entirely different electrochemical behavior than observed for the Co/Bi-POMs (**1**) and (**2**) (Fig. 6).

CV has furthermore proven useful to predict possible WOC activity of POMs in the presence of $[Ru(bpy)_2]^{3+}$ photosensitizer:1if the electrochemical potential of the $[Ru(bpy)_2]^{2+/3+}$ couple is higher than that of the respective metal couple in the POM under consideration, the water oxidation process is thermodynamically favored.[40] In the present POM series, the $[Ru(bpy)_2]^{2+/3+}$ couple is capable of oxidizing the active cobalt sites in Co/Bi-POM (**1**), whereas activation of the cobalt centers in compound (**2**) or the Mn^{2+}/Mn^{3+} redox couple in (**3**) is not possible according to CV results (Fig. 6). Furthermore, the rapidly ascending wave in the anodic part of the voltammogram of (**1**) is consistent with the observed WOC activity, whereas this phenomenon is absent for the catalytically inactive POMs (**2**) and (**3**).

After catalyst stability and suitable electrochemical properties of Co/Bi-POM (**1**) had been established, its role as unique WOC was further investigated with a series of stability tests (Table 2). The results show that the simultaneous presence of (**1**), $Na_2S_2O_8$ and $[Ru(bpy)_3]^{2+}$ under light irradiation exclusively leads to O_2 evolution, which is not observed if any of these four prerequisites is absent. Next, the POM-PS complex of $[Ru(bpy)_3]^{2+}$ and Co/Bi-POM (**1**) was recovered by centrifugation and characterized. Reference POM-PS complex of (**1**) was obtained from the reaction of both components in buffer media or distilled water, and FT-IR spectra confirm the identity of recovered and as-synthesized complex (Fig. 7–8).

A comparison of FT-IR spectra of recovered POM-PS (**1**) complex with pristine PS and POM (Fig. 7) shows characteristic bands in the 1600–1400 cm^{-1} region (1635, 1604, 1500, 1467, 1446, 1428 cm^{-1}) arising from the $[Ru(bpy)_3]^{2+}$ countercation. The intense and broad band around 1067 cm^{-1} (s) with a shoulder at 1184 cm^{-1} (w) is attributed to Si–O vibrations emerging from hydrolysis products of the buffer solution, which are convoluted with the sharp peak of the pristine $[Ru(bpy)_3]^{2+}$ sensitizer at 1161 cm^{-1} (s). In the 900–400 cm^{-1} region, characteristic POM bands are observed (942, 869, 798, 763, 550, 449 cm^{-1}) which underwent an average shift of +20 cm^{-1} compared to pristine POM, probably due to the electrostatic POM-PS interactions. Overlap between POM bands of POM-PS (**1**) complex (620 cm^{-1}, 514 cm^{-1}, 453 cm^{-1}, 418 cm^{-1}) synthesized in water and pristine POM (617 cm^{-1}, 515 cm^{-1}, 453 cm^{-1}, 416 cm^{-1}) is even more accurate (Fig. 8).

Catalytic tests on recycled POM-PS (**1**) complex showed WOC activity only in freshly prepared standard media under irradiation (Table 3). The complex can be recycled twice for O_2 evolution and its activity dropped after further cycles, although FT-IR spectra did not point to significant structural changes (*cf.* Fig. S15†).

The POM-PS (**1**) complex was furthermore characterized with TG measurements which are compared to results for pristine (**1**) in Fig. 9. The initial mass loss of *ca.* 4.7% for both compounds can be ascribed to the associated 10 aqua ligands of the POM moiety. The POM-PS (**1**) complex undergoes a mass loss of 15.3% which is probably due to decomposition of the 2,2'-bipyridine ligands into CO_2 and NO_x and points to the electrostatic attachment of $2/3[Ru(bpy)_3]^{2+}$ molecules per POM polyanion.

Catalytic activity among the POM series

The most striking result emerging from the present study is the drastic difference in WOC activity between the isostructural Co/Bi-POMs (**1**) and (**2**). Given that no indications of substantial instability were observed for either compound, reduction of the Co occupancy of the terminal core positions by 25% in (**2**) is detrimental for its catalytic activity. As far as we know, such a notable influence of subtle disorder differences on the catalytic performance has never been

Table 2 Reference experiments for Co/Bi-POM (**1**) under different catalytic conditions (1 mM $[Ru(bpy)_3]Cl_2$, 5 mM $Na_2S_2O_8$ and 166 μM of catalyst in Na_2SiF_6 (20 mM, pH 5.8)

Catalyst	e^- acceptor	PS	Irradiation	WOC activity
—	$S_2O_8^{2-}$	—	yes	no
—	—	$Ru(bpy)_3^{2+}$	yes	no
—	$S_2O_8^{2-}$	$Ru(bpy)_3^{2+}$	no	no
1	—	—	yes	no
1	$S_2O_8^{2-}$	—	yes	no
1	—	$Ru(bpy)_3^{2+}$	yes	no
1	$S_2O_8^{2-}$	$Ru(bpy)_3^{2+}$	no	no
1	$S_2O_8^{2-}$	$Ru(bpy)_3^{2+}$	yes	yes

Table 3 Reference experiments for recovered POM-PS (**1**) complex suspension under different catalytic conditions (1 mM $[Ru(bpy)_3]Cl_2$, 5 mM $Na_2S_2O_8$ in 20 mM Na_2SiF_6 at pH 5.8)

Catalyst	e^- acceptor	PS	Light	Activity
Recovered **1**	—	—	yes	no
Recovered **1**	$S_2O_8^{2-}$	—	yes	no
Recovered **1**	—	Fresh $Ru(bpy)_3^{2+}$	yes	no
Recovered **1**	$S_2O_8^{2-}$	Fresh $Ru(bpy)_3^{2+}$	no	no
Recovered **1**	$S_2O_8^{2-}$	Fresh $Ru(bpy)_3^{2+}$	yes	yes

reported for POM-based WOCs. Furthermore, this result is in contrast to recent reports on the WOC activity of single-site $[Co^{III}Co^{II}(H_2O)W_{11}O_{39}]^{7-}$ with a disordered catalytic center.[11] Comparison of (1) and (2) suggests at first glance that the terminal $\{Co(H_2O)_3\}$ sites are decisive for WOC activity, whereas the internal $\{M(H_2O)_2\}$ (M = 50% Co, 50% W) sites are less active. As outlined above, the well-defined Co-rich POM $[Bi_2W_{20}Co_2O_{70}(H_2O)_6]^{10-}$ remains difficult to access for reference experiments,[24,25] so that theoretical calculations and isotope labeling experiments are scheduled to assign the precise roles of the different core sites in the water oxidation mechanism.

Meanwhile, electrochemical measurements are a promising pre-screening method for the targeted selection of WOC candidates among the manifold POM motifs as illustrated by predictive CV measurements for (1) and (2) (Fig. 6).

Concerning Mn/Bi-POM (3), its lack of WOC activity does not come as a comparable surprise, because ongoing work on bio-inspired Mn-containing WOC complexes demonstrated that their construction is demanding due to the manifold key criteria for electron transfer and flexibility, which limit the number of known examples.[41,42] Selected molecular Mn-WOCs include $[(bpy)_2Mn(\mu\text{-}O)_2Mn(bpy)_2]^{3+}$ immobilized on clay or mica[43] and a bio-inspired dinuclear manganese complex with imidazole and carboxylate containing ligands.[44] Both compounds already show strong tendencies towards aggregation into higher nuclearities, and consequently, Ca-Mn-oxides have recently emerged as promising solid state Mn-WOCs.[45] Nevertheless, POMs as a "missing link" between molecules and oxide networks remain an attractive target for WOC construction so that the general lack of active Mn-WOCs merits further clarification.

Conclusions

An isostructural series of sandwich-type Co- and Mn-POMs, namely $Na_{10}[\{Co(H_2O)_3\}_2\{CoBi_2W_{19}O_{66}(OH)_4\}]\cdot 37H_2O$ (Co/Bi-POM (1)), $Na_8[Co_{2.5}(H_2O)_6\{Bi_2W_{19.5}O_{66}(OH)_4\}]\cdot 32H_2O$ (Co/Bi-POM (2) and their Mn-containing analogue $Na_6[Mn_{1.5}(H_2O)_6\{Bi_2W_{20.5}O_{68}(OH)_2\}]\cdot 36H_2O$ (Mn/Bi-POM (3)) were obtained from systematic parameter variations of a solution-based synthetic protocol. All POMs were characterized with a variety of analytical methods, and their performance as visible-light-driven water oxidation catalysts (WOCs) was investigated. Extensive parameter screening indicated that a certain extent of M/W-disorder (M = Mn, Co) on the internal and terminal positions, respectively, of the four-membered $M^{2+}|W$ core is strongly favored over the formation of pure M^{2+} metal cores which have, to the best of our knowledge, not yet been reported for this tungstobismutate sandwich-type. Co/Bi-POM (1) displays (1 : 1) Co/W disorder only on the internal sites of the metal core, whereas the external $\{Co(H_2O)_3\}$ sites are fully occupied. In comparison, Co/Bi-POM (2) displays the same disorder pattern on the internal sites together with a (3 : 1) Co/W ratio on the terminal core positions. Mn/Bi-POM (3) also exhibits disorder over the entire core region: the internal positions are mainly occupied with W (90%), whereas the terminal sites are Mn-rich (65%).

The core composition exerts a tremendous influence on the WOC performance, and only Co/Bi-POM (1) exhibits catalytic activity among the series under standard test conditions ($[Ru(bpy)_3]^{2+}$ photosensitizer with $S_2O_8^{2-}$ as sacrificial electron acceptor). Co/Bi-POM (1) performance ranks among the most prominent POM-WOCs reported to date with respect to oxygen yield (96% for 115 μM). Moreover, Co/Bi-POM (1) forms a POM/PS complex with $[Ru(bpy)_3]^{2+}$ which can be recycled for further oxygen evolution runs. Thermogravimetric analyses of the Co/Bi-POM (1)/PS associate indicate that its PS : POM ratio is below values around 4 : 1 as reported by other groups. Further XAS studies on the precise structure of the POM/PS complex are in progress. However, development of neutral or positively charged PS systems would be a more sustainable long-term alternative.

Detailed reference experiments and stability tests indicated that Co/Bi-POM (1) is stable on the timescale of WOC experiments, and no indications for nanoparticle formation through Co^{2+} leaching from the metal core were found. Cyclovoltammetric measurements confirmed the integrity of the newly found POM-WOC, and the redox potentials of all three title POMs in comparison with the electrochemical potential of the $[Ru(bpy)_2]^{2+/3+}$ couple agree well with their experimentally determined WOC activities. This renders CV techniques a useful tool for the selective screening of potential POM-WOC candidates.

Most importantly, the results shed new light on the structure–activity relationships for POM-WOC construction. Comparison of the active WOC Co/Bi-POM (1) with its inactive analogue Co/Bi-POM (2) shows that a subtle difference in the Co occupancy of the terminal positions decides about WOC activity or inactivity. This result opens up new perspectives for investigations into the minimum requirements for POM-WOC construction. If the only terminal core sites were essential for WOC activity, economic single-site POMs would be attractive design targets. As the two Co/Bi-POM end members of the series with (a) fully occupied Co core and (b) Co on terminal sites and W on internal sites could not be preparatively accessed to date, we pursue computational and labeling strategies in parallel to assign the precise roles of the core sites in the water oxidation mechanism. We have furthermore started to investigate the influence of the heteroatom within the lacunary POM shells, and our present results indicate that the presence of a lone pair as in Bi^{3+} exerts a productive influence on the WOC performance.

Our extensive screenings in search of Mn-POMs with WOC activity further underscore the need for SAR. The present study shows a representative example for their elusive character, and additional results will be reported in due course. In the case of Mn/Bi-POM (3), WOC inactivity might be due to the lower Mn occupancy of the terminal sites. However, the general contrast between reported WOC activity of various Mn-based molecular and nano-oxide catalysts on the one hand and the ongoing lack of Mn-POM-WOCs on the other

hand might point to underlying drawbacks associated with the POM shell architecture. Further theoretical and synthetic studies are currently in progress to establish reliable rules for POM-WOC core construction.

Experimental section

Materials and methods

$Na_9[\alpha\text{-}BiW_9O_{33}]\cdot 19.5H_2O$ was prepared and purified according to literature protocols.[25] Tris(2,2'-bipyridyl)dichlororuthenium(II) hexahydrate ($[Ru(bpy)_3]^{2+}$) was purchased (Sigma Aldrich, reagent grade) and recrystallized before use. All other chemicals and salts were commercially purchased with maximum purity levels from commercial suppliers (Sigma Aldrich, TCI).

Synthesis of compounds (1–3)

Co/Bi-POM (**1**) was synthesized according to a literature protocol from the dissolution of freshly prepared $Na_9[\alpha\text{-}BiW_9O_{33}]\cdot 19.5H_2O$ in sodium acetate buffer, followed by the addition of $CoCl_2\cdot 6H_2O$ dissolved in a minimum of distilled water.[24] After heating to 80 °C under reflux, hot filtering and cooling, Co/Bi-POM (**1**) was obtained in phase pure and single crystalline form as violet needle-shaped crystals (yield: 65% based on W). Elemental analysis (%), calc. (found): Bi, 6.72 (7.35); Co, 2.84 (2.77); W, 56.23 (56.0); Na, 3.70 (4.4). Thermogravimetric analysis: one weight loss step in the range of 30–100 °C was observed, corresponding to the loss of hydrating and coordinated water molecules (Fig. 9). IR (ATR-FTIR, cm^{-1}): 930 cm^{-1} (s), 775 cm^{-1} (s), 830 cm^{-1} (w), 664 cm^{-1} (w), 589 cm^{-1} (w), 425 cm^{-1} (w) (Fig. S4†). Intense bands around 450 and 535 nm in the UV/Vis absorption spectrum (Fig. 4) of Co/Bi-POM (**1**) in solution (50 μM) are in a good agreement with other Co^{II} polyoxometalates.[46]

Co/Bi-POM (**2**) was obtained through a slight modification of the above procedure:[24] $Na_9[\alpha\text{-}BiW_9O_{33}]\cdot 19.5H_2O$ was dissolved in distilled water instead of sodium acetate buffer, followed by longer stirring after addition of $CoCl_2\cdot 6H_2O$, heating to 70–80 °C for 60 min and cooling to room temperature. (**2**) was isolated as pink needle-shaped crystals (yield: 82% based on W). Elemental analysis (%), calc. (found): Bi, 6.53 (5.65); Co, 1.84 (1.95); W, 57.5 (60.2); Na, 3.6 (3.87). Thermogravimetric analysis: one weight loss step in the range of 30–100 °C was observed, corresponding to the loss of hydrating and coordinated water molecules (Fig. S16†). IR (ATR-FTIR, cm^{-1}): 938 (s), 953 (w), 823 (s), 789 (w), 733 (w) (Fig. S4†). Intense bands around 450 and 535 nm in the UV/Vis absorption spectrum (Fig. 4) of Co/Bi-POM (**2**) in solution (70 μM) are in a good agreement with other Co^{II} polyoxometalates.[46]

Mn/Bi-POM (**3**) was obtained from $Na_9[\alpha\text{-}BiW_9O_{33}]\cdot 19.5H_2O$ and $MnSO_4\cdot 2H_2O$ in sodium acetate buffer *via* related literature procedures[24] as yellow needle-shaped crystals (yield: 70% based on W). Elemental analysis (%), calc. (found): Bi, 6.65 (6.52); Mn, 1.31 (1.28); W, 59.96 (59.21); Na, 2.20 (3.12). Thermogravimetric analysis: one weight loss step in the range of 30–100 °C was observed, corresponding to the loss of hydrating and coordinated water molecules (Fig. S5†). IR (ATR-FTIR, cm^{-1}): 926 (s), 870 (w), 759 (s), 749 (s), 578 (w) (Fig. S4†). Intense bands lower than 350 nm and around 400 nm in the UV/Vis absorption spectrum (Fig. S9†) of Mn/Bi-POM (**3**) in solution (50 μM) are in a good agreement with other Mn^{II} polyoxometalates.[47] Slight discrepancies in the heavy atom contents found by elemental analysis can be explained in terms of cation disorder as has been frequently observed in polyoxometalate chemistry.

Analytical characterization

Cyclic voltammetry (CV) was performed on a Metrohm 797 VA Computrace instrument with glassy carbon electrode (Metrohm AG, 3 mm diameter) as working electrode and an Ag/AgCl reference electrode. Prior to all measurements, solutions were deaerated with pure N_2. Cyclic voltammograms were obtained in 0.4 M H_2SO_4 at pH 3 and 20 mM Na_2SiF_6/$NaHCO_3$ buffer at pH 5.8 containing the respective polyoxoanion (2.0 mM) at room temperature (scan rate 10–100 mV s^{-1}), to investigate the according redox waves of different metallic centers. The potential domain of the voltammograms is divided into a positive and a negative section (*vs.* Ag/AgCl) for their sequential analysis.

FT-IR spectra were recorded on a Perkin Elmer BXII spectrometer with KBr pellets. Attenuated total reflectance Fourier-transform (ATR-FTIR) spectra were recorded on a Bruker Vertex 70 spectrometer equipped with a Platinum ATR accessory with a diamond crystal. Elemental analyses were performed by Mikroanalytisches Labor Pascher, Remagen, Germany. Thermogravimetric analyses (TGA) were performed on a Netzsch STA 409 CD instrument between 30 and 1000 °C with a heating rate of 10 K min^{-1}. UV/Vis spectra were recorded on a Lambda 650 S Perkin Elmer UV-Visible spectrometer in the range 300–800 nm using a Quartz SUPRASIL precision cell (10 mm). TG measurements were performed on a Netzsch STA 449 C between 25 and 800 °C with a heating rate of 10 K min^{-1} in nitrogen atmosphere.

X-ray crystallography

Suitable crystals of (**1**)–(**3**) for X-ray analysis were all coated with Paratone-N oil and mounted inside a small fiber loop placed in a cooled N_2 gas flow at 183 K. Data collections of (**1**), (**2**) and (**3**) were performed on an Oxford Xcalibur Ruby CCD single-crystal diffractometer (Mo K_α radiation, λ = 0.71073 Å). Routine Lorentz and polarization corrections were applied, and an absorption correction was applied using the program CrysAlis (multi-scan).[48] Structural analysis was performed with the Win-GX software package.[49] Direct methods were used to locate heavy metal atoms (SHELXS-97) and the remaining atoms were located from successive Fourier maps (SHELXL-97).[50]

Further details on the crystal structure investigations may be obtained from the Fachinformationszentrum Karlsruhe, D-76344 Eggenstein-Leopoldshafen, Germany (Fax: +49 7247 808 666; email: crysdata@fiz-karlsruhe.de), on quoting the

depository numbers CSD-426302 (for Co/Bi-(1)), CSD-426303 (for Co/Bi-(2)), and CSD-426304 (for Mn/Bi-(3)).

Visible-light-driven water oxidation

Water oxidation experiments were performed in a 10 mL headspace vial sealed with an aluminum crimp cap with a rubber septum (PTFE). Reaction mixtures were prepared under dark conditions as follows: 8 mL of a solution containing 1 mM $[Ru(bpy)_3]Cl_2$, different concentrations of $Na_2S_2O_8$ (2 to 7 mM), 20 mM $Na_2SiF_6/NaHCO_3$ buffer at pH 5.8 (freshly prepared), and the according concentration of catalyst concentration were added to a glass vessel. The solution was deaerated by purging with helium (6.0 purity) for 30 min.

Oxygen evolution was measured both in solution and in the headspace using an Oxygen Sensor (OX-N) Clark electrode (Unisense). Constant temperature was maintained with a mineral insulated thermosensor (2 mm tip diameter, TP2000, Unisense).

After purging an initial 100 μL sample of the headspace was injected into a gas chromatograph as background reference for the GC calibration. Gas chromatograms were recorded using an Agilent Technologies 7820A gas chromatograph with helium as the carrier gas and a 3 m × 2 mm packed molecular sieve 13X 80–100 column to separate O_2 and N_2. The oven was operated isothermally at 80 °C. Analysis of the headspace was performed by taking 100 μL samples with a Hamilton (1825 RN) gas-tight microliter syringe. Gases were detected using a thermal conductivity detector (Varian) operated at 200 °C. Contamination of the headspace by air was constantly quantified by measuring the N_2 peak on GC chromatograms. Calibration was performed by injection of known quantities of pure oxygen diluted in the same headspace vial containing the same volume and concentration of Na_2SiF_6 as used for the measurements.

After background calibration of the GC, the Clark-type O_2 probe was introduced into the catalytic vessel, first in the headspace until the signal remained constant, and afterwards below the liquid surface accordingly.

Signals were first calibrated using the normal procedure supplied for the applied electrode model. After complete aeration of the water (5 min of vigorous bubbling) in the Unisense calibration chamber CAL300, the gas stream was turned off and the saturation point for the calibration line for atmospheric partial pressure was added. Background calibration was performed with an anoxic solution prepared from sodium ascorbate and NaOH. Controlled stirring (500 rpm) was applied throughout all experiments.

Data collection was performed with the SensorTrace software from Unisense, with a frequency of 1 data point per sec for both probes (T and O_2). After a constant signal for the O_2 sensor was recorded, the catalytic reaction was initiated by exposing the reaction vessel to the light of a 470 nm high flux LED from Rhopoint Components LTD. The LED power was determined as 26.1 mW cm^{-2}.

Catalyst recycling

Catalysts were recovered from reaction mixtures containing 1 mM $[Ru(bpy)_3]Cl_2$, 5 mM $Na_2S_2O_8$ and the given concentration of WOC in Na_2SiF_6 aqueous media (20 mM, pH 5.8). The solution was kept under LED irradiation for the catalytic reaction time and a red precipitate was obtained after centrifugation. The obtained powder was washed twice with distilled water, dried in N_2 atmosphere and characterized with FT-IR spectroscopy, TG and XRD.

Acknowledgements

This work was supported by the Swiss National Science Foundation (SNSF Professorship PP00P2_133483/1 and Sinergia Grant No. CRSII2_136205/1) and by the University of Zurich (Institute of Inorganic Chemistry and UFSP LightChEC). We thank PD Dr. Bernhard Spingler for discussions on the crystal structures.

Notes and references

1 (*a*) Y. Tachinaba, L. Vayssieres and J. R. Durrant, *Nat. Photonics*, 2012, **6**, 511–518; (*b*) R. J. Cogdell, A. T. Gardiner and L. Cronin, *Philos. Trans. R. Soc. London, Ser. A*, 2012, **370**, 3819–3826; (*c*) J. Barber, *Chem. Soc. Rev.*, 2009, **38**, 185–196; (*d*) D. G. Nocera, *Acc. Chem. Res.*, 2012, **45**, 767–776; (*e*) K. J. Young, L. A. Martini, R. L. Milot, R. C. Snoeberger, V. S. Batista, C. A. Schmuttenmaer, R. H. Crabtree and G. W. Brudvig, *Coord. Chem. Rev.*, 2012, **256**, 2503–2520.

2 (*a*) G. C. Dismukes, R. Brimblecombe, G. A. N. Felton, R. S. Pryadun, J. E. Sheats, L. Spiccia and G. F. Swiegers, *Acc. Chem. Res.*, 2009, **42**, 1935–1943; (*b*) E. S. Andreiadis, M. Charavot-Kerlidou, M. Fontecave and V. Artero, *Photochem. Photobiol.*, 2011, **87**, 946–964; (*c*) A. Savini, G. Bellachioma, G. Ciancaleoni, C. Zuccaccia, D. Zuccaccia and A. Macchioni, *Chem. Commun.*, 2010, **46**, 9218–9219; (*d*) I. Rivalta, G. W. Brudvig and V. S. Batista, *Curr. Opin. Chem. Biol.*, 2012, **16**, 11–18.

3 (*a*) *Polyoxometalates: from Platonic Solids to Antiretroviral Activity* ed. M. T. Pope and A. Müller), Kluwer, Dordrecht, 1994; (*b*) U. Kortz, A. Müller, J. van Slageren, J. Schnack, N. S. Dalal and M. Dressel, *Coord. Chem. Rev.*, 2009, **253**, 19–20; (*c*) *Chem. Rev.*, Special Issue on Polyoxometalates, ed. L. Hill, 1998, 98, pp. 1–389; (*d*) L. Cronin, *Angew. Chem., Int. Ed.*, 2006, **45**, 3576–3578; (*e*) *Polyoxometalate Molecular Science*, ed. J. J. Borras-Almenar, E. Coronado, A. Müller and M. T. Pope, Kluwer, Dordrecht, The Netherlands, 2004; (*f*) D.-L. Long, E. Burkholder and L. Cronin, *Chem. Soc. Rev.*, 2007, **36**, 105–121; (*g*) E. Cadot, M. N. Sokolov, V. P. Fedin, C. Simonnet-Jegat, S. Floquet and F. Secheresse, *Chem. Soc. Rev.*, 2012, **41**, 7335–7353.

4 (*a*) N. D. Morris and T. E. Mallouk, *J. Am. Chem. Soc.*, 2002, **124**, 11114–11121; (*b*) Y. V. Geletii, B. Botar, P. Kögerler, D. A. Hillesheim, D. G. Musaev and C. L. Hill, *Angew. Chem., Int. Ed.*, 2008, **47**, 3896–3899; (*c*) Y. V. Geletii,

C. Besson, Y. Hou, Q. Yin, D. G. Musaev, D. Quinonero, R. Cao, K. I. Hardcastle, A. Proust, P. Kögerler and C. L. Hill, *J. Am. Chem. Soc.*, 2009, **131**, 17360–17370; (*d*) C. Besson, Z. Huang, Y. V. Geletii, S. Lense, K. I. Hardcastle, D. G. Musaev, T. Lian, A. Proust and C. L. Hill, *Chem. Commun.*, 2010, **46**, 2784–2786; (*e*) M. Orlandi, R. Argazzi, A. Sartorel, M. Carraro, G. Scorrano, M. Bonchio and F. Scandola, *Chem. Commun.*, 2010, **46**, 3152–3154; (*f*) F. Puntoriero, G. La Ganga, A. Sartorel, M. Carraro, G. Scorrano, M. Bonchio and S. Campagna, *Chem. Commun.*, 2010, **46**, 4725–4727; (*g*) Q. Yin, J. M. Tan, C. Besson, Y. V. Geletii, D. G. Musaev, A. E. Kuznetsov, Z. Luo, K. I. Hardcastle and C. L. Hill, *Science*, 2010, **328**, 342–345; (*h*) Z. Huang, Z. Luo, Y. V. Geletii, J. W. Vickers, Q. Yin, D. Wu, Y. Hou, Y. Ding, J. Song, D. G. Musaev, C. L. Hill and T. Lian, *J. Am. Chem. Soc.*, 2011, **133**, 2068–2071; (*i*) A. Sartorel, M. Truccolo, S. Berardi, M. Gardan, M. Carraro, F. M. Toma, G. Scorrano, M. Prato and M. Bonchio, *Chem. Commun.*, 2011, **47**, 1716–1718; (*j*) R. N. Biboum, C. P. N. Njiki, G. Zhang, U. Kortz, P. Mialane, A. Dolbecq, I. M. Mbomekalle, L. Nadjo and B. Keita, *J. Mater. Chem.*, 2011, **21**, 645–650; (*k*) M. Murakami, D. Hong, T. Suenobu, S. Yamaguchi, T. Ogura and S. Fukuzumi, *J. Am. Chem. Soc.*, 2011, **133**, 11605–11613.

5 (*a*) H. Lv, Y. V. Geletii, C. Zhao, J. G. Vickers, G. Zhu, Z. Luo, J. Song, T. Lian, D. G. Musaev and C. L. Hill, *Chem. Soc. Rev.*, 2012, **41**, 7572–7589; (*b*) A. Sartorel, M. Bonchio, S. Campagna and F. Scandola, *Chem. Soc. Rev.*, 2013, **42**, 2262–2280; (*c*) R. Sivakumar, J. Thomas and M. Yoon, *J. Photochem. Photobiol., C*, 2012, **13**, 277–298.

6 (*a*) R. H. Crabtree, *Chem. Rev.*, 2012, **112**, 1536–1554; (*b*) A. Savini, P. Belanzoni, G. Bellachioma, C. Zuccaccia, D. Zuccaccia and A. Macchioni, *Green Chem.*, 2011, **13**, 3360–3374; (*c*) A. Singh, R. K. Hocking, S. L.-Y. Chang, B. M. George, M. Fehr, K. Lips, A. Schnegg and L. Spiccia, *Chem. Mater.*, 2013, **25**, 1098–1108.

7 G. Zhu, E. N. Glass, C. Zhao, H. Lv, J. W. Vickers, Y. V. Geletii, D. G. Musaev, J. Song and C. L. Hill, *Dalton Trans.*, 2012, **41**, 13043–13049.

8 (*a*) Q. Yin, J. M. Tan, C. Besson, Y. V. Geletii, D. G. Musaev, A. E. Kuznetsov, Z. Luo, K. I. Hardcastle and C. L. Hill, *Science*, 2010, **328**, 342–345; (*b*) M. Orlandi, R. Argazzi, A. Sartorel, M. Carraro, G. Scorrano, M. Bonchio and F. Scandola, *Chem. Commun.*, 2010, **46**, 3152–3154.

9 (*a*) G. Zhu, Y. V. Geletii, J. Song, C. Zhao, E. N. Glass, J. Bacsa and C. L. Hill, *Inorg. Chem.*, 2013, **52**, 1018–1024; (*b*) H. Lv, J. Song, Y. V. Geletii, W. Guo, J. Bacsa and C. L. Hill, *Eur. J. Inorg. Chem.*, 2013, 1720–1725.

10 D. Guo, S. Teng, Z. Liu, W. You and L. Zhang, *J. Cluster Sci.*, 2013, **34**, 549–558.

11 F. Song, Y. Ding, B. Ma, C. Wang, Q. Wang, X. Du, S. Fu and J. Song, *Energy Environ. Sci.*, 2013, **6**, 1170–1184.

12 S. Tanaka, M. Annaka and K. Sakai, *Chem. Commun.*, 2012, **48**, 1653–1655.

13 P. E. Car, M. Guttentag, K. K. Baldridge, R. Alberto and G. R. Patzke, *Green Chem.*, 2012, **14**, 1680–1688.

14 J. Song, Z. Luo, H. Zhu, Z. Huang, T. Lian, A. L. Kaledin, D. G. Musaev, S. Lense, K. I. Hardcastle and C. L. Hill, *Inorg. Chim. Acta*, 2010, **363**, 4381–4386.

15 K. Heussner, K. Peuntinger, N. Rockstroh, L. C. Nye, I. Ivanovic-Burmazovic, S. Rau and C. Streb, *Chem. Commun.*, 2011, **47**, 6852–6854.

16 M. Natali, M. Orlandi, S. Berardi, S. Campagna, M. Bonchio, A. Sartorel and F. Scandola, *Inorg. Chem.*, 2012, **51**, 7324–7331.

17 J. Gao, S. Cao, Q. Tay, Y. Liu, L. Yu, K. Ye, P. C. S. Mun, Y. Li, G. Rakesh, S. C. J. Loo, Z. Chen, Y. Zhao, C. Xue and Q. Zhang, *Sci. Rep.*, 1853, **2013**(3), 1–5.

18 J. Stracke and R. J. Finke, *J. Am. Chem. Soc.*, 2011, **133**, 14872–14875.

19 M. Natali, S. Berardi, A. Sartorel, M. Bonchio, S. Campagna and F. Scandola, *Chem. Commun.*, 2012, **48**, 8808–8810.

20 J. J. Stracke and R. G. Finke, *ACS Catal.*, 2013, **3**, 1209–1219.

21 J. Soriano-López, S. Goberna-Ferrón, L. Vigara, J. J. Carbó, J. M. Poblet and J. R. Galán-Mascarós, *Inorg. Chem.*, 2013, **52**, 4753–4755.

22 N. S. McCool, D. M. Robinson, J. E. Sheats and G. C. Dismukes, *J. Am. Chem. Soc.*, 2011, **133**, 11446–11449.

23 S. Piccinin, A. Sartorel, G. Aquilanti, A. Goldoni, M. Bonchio and S. Fabris, *Proc. Natl. Acad. Sci. U. S. A.*, 2013, **110**, 4917–4922.

24 C.-Y. Sun, S. X. Liu, C. L. Wang, L. H. Xie, C.-D. Zhang, B. Gao and E.-B. Wang, *J. Coord. Chem.*, 2007, **60**, 567–579.

25 I. Loose, E. Droste, M. Bösing, H. Pohlmann, M. H. Dickman, C. Rosu, M. T. Pope and B. Krebs, *Inorg. Chem.*, 1999, **38**, 2688–2694.

26 I. D. Brown and D. Altermatt, *Acta Crystallogr., Sect. B: Struct. Sci.*, 1985, **41**, 244–247.

27 M. Piepenbrink, D. Drewes and B. Krebs, *ICSD 391152, private communication*, 2002.

28 (*a*) L. Ruhlmann, L. Nadjo, J. Canny, R. Contant and R. Thouvenot, *Eur. J. Inorg. Chem.*, 2002, 975–986; (*b*) G. G. Gao, L. Xu, W. Wang, X. Shu Qu, X. Liu and Y. Y. Yang, *Inorg. Chem.*, 2008, **47**, 2325–2333.

29 S. Goberna-Ferron, L. Vigara, J. Soriano-Lopez and R. Galán-Mascarós, *Inorg. Chem.*, 2012, **51**, 11707–11715.

30 (*a*) Y. Z. Voloshina, O. A. Varzatskii, A. S. Belova, Z. A. Starikovaa, A. V. Dolganova, V. V. Novikova and Y. N. Bubnov, *Inorg. Chim. Acta*, 2011, **370**, 322–332; (*b*) J. B. Serra, I. Todorut, N. C. Pastor, J. P. Server-Carrió, L. C. W. Baker and R. Accrete, *Synth. React. Inorg. Met.-Org. Chem.*, 1995, **25**(6), 869–882.

31 (*a*) B. S. Bassil, M. Ibrahim, S. S. Mal, A. Suchopar, R. N. Biboum, B. Keita, L. Nadjo, S. Nellutla, J. van Tol, N. S. Dalal and U. Kortz, *Inorg. Chem.*, 2010, **49**, 4949–4959; (*b*) D. J. Wasylenko, C. Ganesamoorthy, J. Borau Garcia and J. P. Berlinguette, *Chem. Commun.*, 2012, **48**, 2107–2109.

32 (*a*) K. Nomita, M. Miwa, R. Kobayashi and M. Aiso, *Bull. Chem. Soc. Jpn.*, 1981, **54**, 2983–2987; (*b*) N. K. Kala Raja, V. G. Puranikb, C. Gopinathana and A. V. Ramaswamy, *Appl. Catal., A*, 2003, **256**, 265–273.

33 M. Lebrini, I. M. Mbomekalle, A. Dolbecq, J. Marrot, P. Berthet, J. Ntienoue, F. S. Secheresse, J. Vigneron and A. Etcheberry, *Inorg. Chem.*, 2011, **50**, 6437–6448.
34 Y. Liu, B. Liu, G. Xue, H. Hu, F. Fu and J. Wang, *Dalton Trans.*, 2007, 3634–3639.
35 (*a*) X. Y. Zhang, M. T. Pope, M. R. Chancet and J. B. Jameson, *Polyhedron*, 1995, **14**, 1381–1392; (*b*) I. Bar-Nahum, H. Cohen and R. Neumann, *Inorg. Chem.*, 2003, **42**, 3677–3684.
36 A. Sartorel, M. Bonchio, S. Campagna and F. Scandola, *Chem. Soc. Rev.*, 2013, **42**, 2262–2280.
37 P. K. Ghosh, B. S. Brunschwig, M. Chou, C. Creutz and N. J. Sutin, *J. Am. Chem. Soc.*, 1984, **106**, 4772–4779.
38 (*a*) Y. V. Geletii, C. Besson, Y. Hou, Q. Yin, D. G. Musaev, D. Quinonero, R. Cao, K. I. Hardcastle, A. Proust, P. Kögerler and C. L. Hill, *J. Am. Chem. Soc.*, 2009, **131**, 17360–17370; (*b*) G. S. Fink, *Angew. Chem., Int. Ed.*, 2008, **47**, 5888–5890; (*c*) Z. Huang, Z. Luo, Y. V. Geletii, J. V. Vickers, Q. Yin, Y. W. Wu, Y. Ding, J. Song, D. G. Musaev, C. L. Hill and T. Lian, *J. Am. Chem. Soc.*, 2011, **133**, 2068–2071; (*d*) A. Sartorel, M. Carraro, G. Scorrano, R. De Zorzi, S. Geremia, N. D. McDaniel, S. Bernhard and M. Bonchio, *J. Am. Chem. Soc.*, 2008, **130**, 5006–5007.
39 A. Sartorel, M. Truccolo, S. Berardi, M. Gardan, M. Carraro, F. M. Toma, G. Scorrano, M. Prato and M. Bonchio, *Chem. Commun.*, 2011, **47**, 1716–1718.
40 M. Natali, S. Berardi, A. Sartorel, M. Bonchio, S. Campagna and F. Scandola, *Chem. Commun.*, 2012, **48**, 8808–8810.
41 M. Wiechen, H.-M. Berends and P. Kurz, *Dalton Trans.*, 2012, **41**, 21–31.
42 (*a*) L. Sun, L. Hammarström, B. Åkermark and S. Styring, *Chem. Soc. Rev.*, 2001, **30**, 36–49; (*b*) P. Kurz, G. Berggren, M. Anderlund and S. Styring, *Dalton Trans.*, 2007, 4258–4261.
43 M. Yagi and K. Narita, *J. Am. Chem. Soc.*, 2004, **126**, 8084–8085.
44 E. A. Karlsson, B.-L. Tee, T. Åkermark, E. V. Johnston, M. D. Kärkäs, J. Sun, Ö. Hansson, J.-E. Bäckvall and B. Åkermark, *Angew. Chem., Int. Ed.*, 2011, **50**, 11715–11718.
45 M. M. Najafpour, T. Ehrenberg, M. Wiechen and P. Kurz, *Angew. Chem., Int. Ed.*, 2010, **49**, 2233–2237.
46 (*a*) B. J. Johnson and A. Stein, *Inorg. Chem.*, 2001, **40**, 801–808; (*b*) N. K. Kala Raj, V. G. Puranik, C. Gopinathan and A. V. Ramaswamy, *Appl. Catal., A*, 2003, **256**, 265–273.
47 K. Patel, P. Shringarpure and A. Patel, *Transition Met. Chem.*, 2010, **36**, 171–177.
48 *Oxford Diffraction CrysAlis CCD and CrysAlis RED*, Oxford Diffraction Ltd., Abingdon, UK, 2005.
49 L. J. Farrugia, *J. Appl. Crystallogr.*, 1999, **32**, 837–851.
50 G. M. Sheldrick, *SHELX97*, Programs for Crystal Structure Analysis; Release 97–2, University of Göttingen, Göttingen, Germany, 1997.